Lightweight, Superelastic, and Mechanically Flexible Graphene/Polyimide Nanocomposite Foam for Strain Sensor Application

Yuyang Qin,[†,§] Qingyu Peng,[†,‡,§] Yujie Ding,[†] Zaishan Lin,[†] Chunhui Wang,[†] Ying Li,[†] Fan Xu,[†] Jianjun Li,[†] Ye Yuan,[†] Xiaodong He,[*,†] and Yibin Li[*,†]

[†]Center for Composite Materials and Structures and [‡]Division of Aircraft Dynamics and Control, School of Astronautics, Harbin Institute of Technology, Harbin 150080, P. R. China. [§]These authors contributed equally.

ABSTRACT The creation of superelastic, flexible three-dimensional (3D) graphene-based architectures is still a great challenge due to structure collapse or significant plastic deformation. Herein, we report a facile approach of transforming the mechanically fragile reduced graphene oxide (rGO) aerogel into superflexible 3D architectures by introducing water-soluble polyimide (PI). The rGO/PI nanocomposites are fabricated using strategies of freeze casting and thermal annealing. The resulting monoliths exhibit low density, excellent flexibility, superelasticity with high recovery rate, and extraordinary reversible compressibility. The synergistic effect between rGO and PI endows the elastomer with desirable electrical conductivity, remarkable compression sensitivity, and excellent durable stability. The rGO/PI nanocomposites show potential applications in multifunctional strain sensors under the deformations of compression, bending, stretching, and torsion.

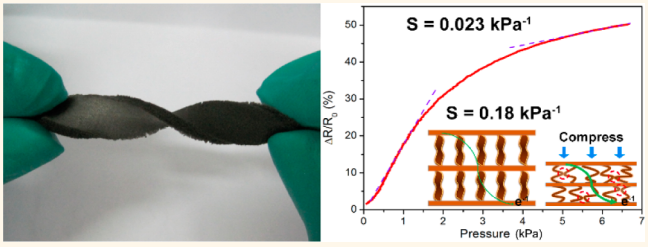

KEYWORDS: graphene · polyimide · mechanically flexible · superelastic · strain sensor

Graphene is a robust two-dimensional (2D) sheet-like allotrope of carbon.[1] It exhibits fascinating electrical, mechanical, and thermal properties.[2,3] These exceptional properties endow it great potential as a unique nanoscale building block for the construction of macroscopic 3D monoliths for a wide range of applications. To date, several methods have been developed to fabricate 3D interconnected structures of graphene to exploit its remarkable integrated properties such as self-gelation,[4−7] freeze casting,[8−11] chemical vapor deposition (CVD),[12,13] and *in situ* unzipping carbon nanotubes sponge.[14] However, these reported graphene foams or aerogels undergo significant plastic deformation or brittle mechanical performance when suffering from cyclic strain of compression, bending, stretching, and torsion. These results restrict the widespread applications of 3D graphene macroscopic monoliths. Constructing graphene foam with excellent mechanical properties is still a big challenge. To enhance the mechanical properties, especially the flexibility of graphene sponge, several attempts have been proposed. For example, Jiang *et al.* have demonstrated a self-assemble strategy of graphene oxide (GO) on the internal skeleton of polymer to produce 3D porous graphene foams.[15] Yu *et al.* reported the fabrication of macroscopic graphene frameworks by a fractured microstructure design in a graphene-nanosheet-wrapped polyurethane (PU) sponge.[16] Liao *et al.* introduced a two-step process for the formation of graphene foams, in which the PU foam was dip-coated with GO, and subsequently the polymer skeleton was pyrolyzed, leaving pure graphene foam.[17] The above-mentioned 3D graphene foams exhibit good electrical conductivity and fine mechanical integrity. Such developments have opened up new avenues for the preparation of 3D networked graphene macrostructures, which are desirable for applications as pressure sensors. However, the pore morphology and mechanical properties of these foams or

* Address correspondence to liyibin@hit.edu.cn, hexd@hit.edu.cn.

Received for review May 7, 2015 and accepted August 22, 2015.

Published online August 24, 2015
10.1021/acsnano.5b02781

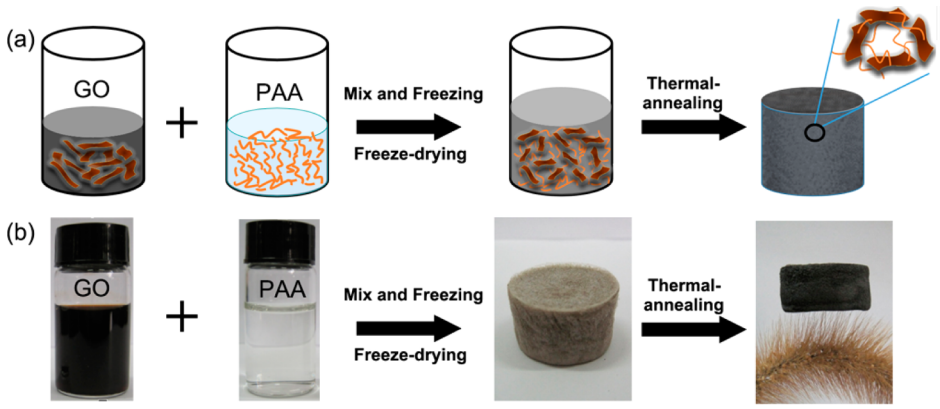

Figure 1. (a) Schematic illustration of the two-step fabrication process of rGO/PI nanocomposite. GO solution and PAA solution (water-soluble PI precursor) were mixed together, and then the mixture was successively subjected to freeze-drying and thermal annealing to form a 3D interconnecting rGO/PI architecture. (b) Digital photographs of GO suspension, PAA solution, GO/PAA monolith, and rGO/PI nanocomposite, which can rest on the green bristlegrass.

sponges mostly depend on the framework of polymer. On the other hand, the graphene may peel off from the internal walls of sponge after numerous compression cycles because the adhesive force (van der Waals or $\pi-\pi$ interaction) between graphene and the wall is very weak. This will result in sensor failure. Owing to superior elastic and flexible attributes, outstanding thermal stability, and high glass transition temperature, polyimide (PI) is considered as an attractively high-performance engineering polymer.[18] Most importantly, the precursor of PI can be transformed into aqueous solution by chemical modification. Inspired by this, water-soluble PI was chosen to enhance the elastic and flexible properties of GO aerogels in this work. Here, we demonstrate a novel approach to fabricate a lightweight, superelastic, and mechanically flexible nanocomposite foam by introducing water-soluble PI precursor[19] into GO sheets. The flexible nanocomposite foam is very promising as a strain sensor.

RESULTS AND DISCUSSION

The overall preparation procedure of reduced GO (rGO)/PI nanocomposites is schematically illustrated in Figure 1. Briefly, fluid solutions of GO[20] and poly(amic acid) (PAA, PI precursor)[19] with controlled concentrations were mixed together, and then the homogeneous mixture was further treated by a cryodesiccation method. Finally, the resulting monolith was subjected to thermal annealing in argon atmosphere at 300 °C to form the rGO/PI nanocomposite.[33] The freestanding and mechanically stable rGO/PI nanocomposite reveals a 3D interconnecting architecture (Figure 1a) and a low density (10 mg cm^{-3}), which can rest on the tip of green bristle grass (Figure 1b). Because of the simple and readily accessible synthesis process, rGO/PI nanocomposites with desired shapes such as cylinders, cubes, and ribbons were facilely prepared (Figure S3). For comparison, pure rGO aerogels and normal PI monoliths without the addition of GO were also fabricated under the same procedure.

Microstructures and morphologies of rGO aerogel, PI monolith, and rGO/PI nanocomposite were imaged at different magnifications using scanning electron microscopy (SEM) (Figure 2a−c). The microstructure analysis of rGO aerogel exhibits a randomly oriented porous structure, which is constructed by interconnected rGO sheets *via* partial overlapping by $\pi-\pi$ interactions in a 3D configuration (Figure 2a).[21] The assembly and organization of the aerogel were driven by the interaction forces between GO sheets, which revealed the decrease of electrostatic repulsions and the enhancement of $\pi-\pi$ attraction during the reduction procedure triggered by thermal annealing. The high-magnification SEM image in Figure 2, panel a, exhibits thin pore walls of rGO aerogel, where the wrinkles and folds of rGO sheets can be observed. Owing to the rearrangement effect of freeze casting,[22] the SEM observation of PI monolith shows highly lamellar structures with struts connecting the adjacent layers (Figure 2b), in which the layer spacing is from hundreds of nanometers to tens of micrometers. As for the rGO/PI nanocomposite, it is worth noting that the unique "layer-strut" bracing architecture is maintained with the increase of monolayer thickness and layer spacing (Figure 2c). By zooming in on a layer or a strut of the 3D binary-network structure, the image presents the characteristics of wrinkles and ripples similar to rGO sheets. It reveals the strong interplay between rGO sheets and PI building blocks. The remarkable "layer-strut" skeletons of rGO/PI nanocomposite contribute to the efficient load-transfer between rGO sheets and PI building blocks under mechanical deformation and lead to an enhancement of mechanical properties. To further investigate the microstructures of GO nanosheets and rGO nanosheets after PI coating, transmission electron microscopy (TEM) images of original GO nanosheets and as-prepared rGO/PI nanocomposites (PI 40 wt %) were depicted in Figure S1. The TEM observations reveal some ripples and wrinkles in carpet-like pristine GO nanosheets. For comparison, the rGO

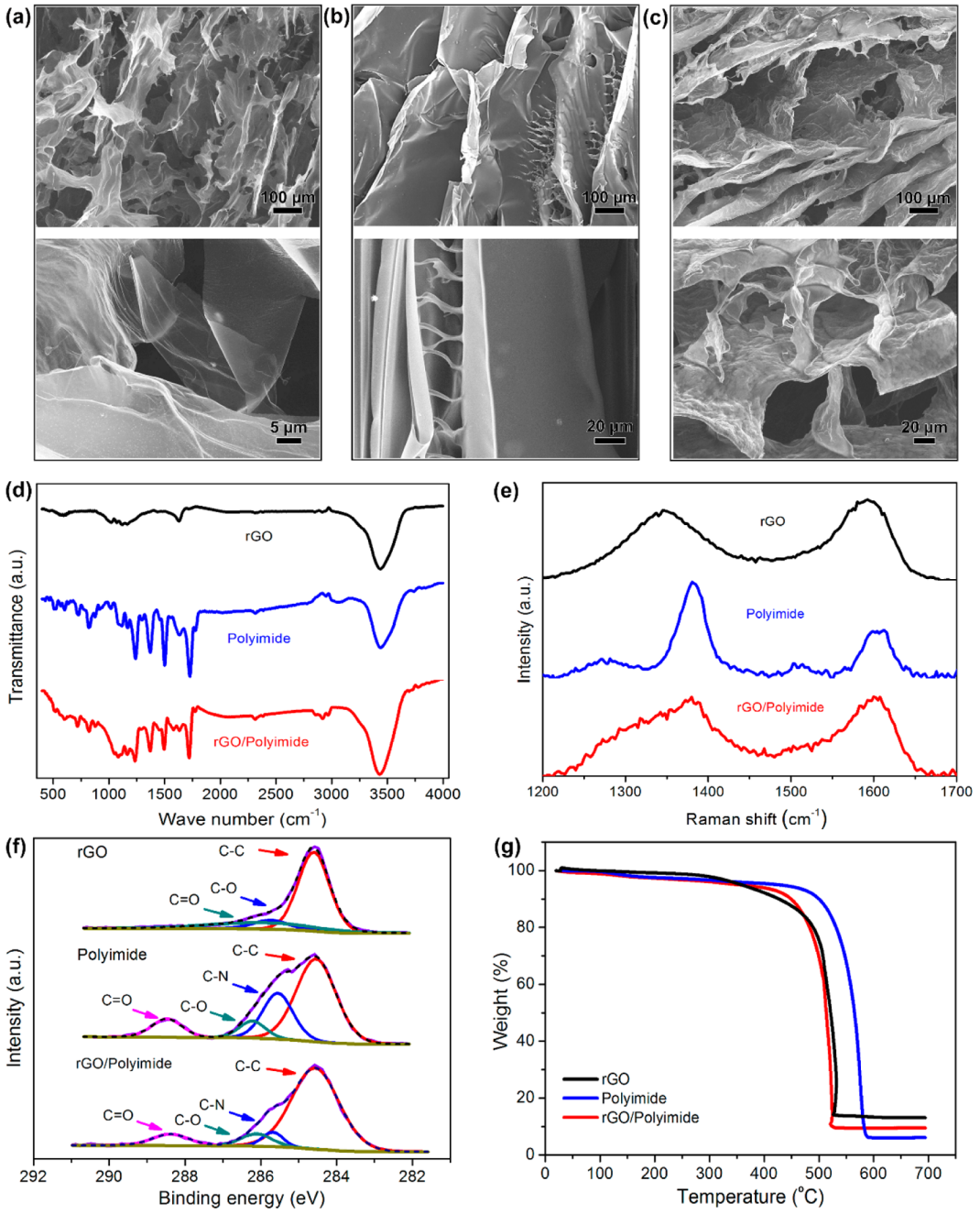

Figure 2. (a–c) SEM images of rGO aerogel, PI monolith, and rGO/PI nanocomposite at low and high magnification. (d) FT-IR, (e) Raman, (f) XPS, and (g) TGA data of rGO, PI, and rGO/PI samples.

nanosheets after PI coating exhibit an encapsulating morphology with many darker spots visible on the surface, indicating the successful introduction of water-soluble PI.

To investigate the chemical structure and possible interactions between rGO sheets and PI chains in the nanocomposite, spectroscopic analyses were adopted using Fourier transform infrared (FT-IR), Raman spectroscopy, and X-ray photoemission spectroscopy (XPS). As expected in Figure 2, panel d, the FT-IR spectra of rGO show two prominent characteristic peaks located at 3435 and 1621 cm^{-1}, respectively. These are attributed to the broad and intense O–H stretching vibration and aromatic C=C bonds skeletal stretching vibrations of unoxidized graphitic domains. In comparison with GO, the characteristic peaks of the oxidation groups of rGO decrease, reflecting the partial reduction of GO (Figure S2d). As for the normal PI monolith, the characteristic peaks at 1726 and 1773 cm^{-1} are assigned to the imide C=O symmetric and asymmetric stretches. The peaks of C–N stretching vibration (1371 cm^{-1}) and C=C stretching vibration (1503 cm^{-1}) can also be observed, in consistence with the presence of PI.[19] In the FT-IR spectrum of the rGO/PI

nanocomposite, however, the characteristic peaks at 1726, 1503, and 1371 cm^{-1} assigned to C═O, C═C, and C−N stretching vibration are shifted to 1706, 1483, and 1359 cm^{-1}, respectively. The main interaction force between GO and PAA can be attributed to strong hydrogen bonds and interfacial interactions.[23] Notably, it can be expected that pendant hydroxyl groups across the surfaces and sides of GO nanosheets could form hydrogen bonds with the carbonyl groups of PAA. In addition, the surface chemistry of GO nanosheets, which contains high surface area and nanoscale surface roughness, can contribute to the strong interaction between GO and PAA. These should be the main reasons for the shift of peaks in FT-IR. The Raman spectra patterns of rGO, PI, and rGO/PI samples are presented in Figure 2, panel e. The rGO mainly exhibits two remarkable bands at around 1347 and 1586 cm^{-1}, which correspond to the D-band and G-band of graphitic carbon, respectively. As for the PI sample, the peak at 1381 cm^{-1} indicates the C−N stretching vibration of the imide ring, while the characteristic Raman features of ring vibration of carboxylic acid (1601 cm^{-1}) and aromatic imide ring in dianhydride part (1612 cm^{-1}) can also be observed. However, in the rGO/PI nanocomposite, the D-band of GO (1347 cm^{-1}) and the C−N stretching vibration band of PI (1381 cm^{-1}) overlap each other to form a broad and intense band. Meanwhile, another broad peak at 1600 cm^{-1} is due to the overlapping of the G-band of GO (1586 cm^{-1}) and the ring vibration of PI (1601 and 1612 cm^{-1}).[24] The elemental compositions of rGO/PI nanocomposite and PI were exhibited by wide-scan XPS profiles (Figure S2b). Both PI and rGO/PI nanocomposite contain significant peaks of C 1s (284.6 eV), N 1s (400 eV), and O 1s (532 eV), while the N 1s peak decreases in rGO/PI nanocomposite.[25] In the C 1s spectra of rGO (Figure 2f), three configurations centering at 284.6 eV (C═C/C−C), 286.6 eV (C−O), and 287.8 eV (C═O) can be deconvoluted. Compared with GO, the peak intensity of C−C rises dramatically, while oxidation groups (C═O, C−O−C, O−C═O) decrease sharply (Figure S2c). The low intensities of the oxygen-contained peaks, which are accompanied by the increase of the sp^2 carbon peak, reveal a high degree of reduction.[26] As for the sample of PI, the C 1s spectrum can be split into four components at 284.6 eV (C═C/C−C), 285.5 eV (C−N), 286.3 eV (C−O), and 288.6 eV (C═O).[27] However, in the case of the rGO/PI nanocomposite, the peak intensities of C−N, C−O, and C═O decrease, while that of sp^2 carbon peak increases, suggesting the strong interactions of rGO and PI. The thermal stabilities of rGO aerogel, PI monolith, and rGO/PI composite were evaluated by thermogravimetric analysis (TGA), as shown in Figure 2, panel g. The onset of rGO decomposition is at around 360 °C, and the decomposition continues until 530 °C with the weight loss of 96%. Compared with GO, the rGO expresses high thermal stability (Figure S2a). In the TGA curve of PI, the onset degradation temperature is at around 460 °C, and the residual weight at 500 °C is estimated to be 90%. With the addition of PI, rGO/PI nanocomposite exhibits an increase in thermal stability presumably due to the strong interplay between rGO and PI. The rGO/PI nanocomposite expresses a similar pattern of weight loss to the rGO sample, but its decomposition temperature is higher (around 420 °C). These evidences indicate that there are strong interactions between rGO and PI that substantially influence on the mechanical and chemistry properties of the nanocomposites.

To assess the mechanical properties of the rGO/PI nanocomposite, especially the recyclable compressibility, a set of compressive tests was quantitatively conducted. As shown in Figure 3, panel a, we measured the compressive stress (σ) as a function of strain (ε) of rGO/PI nanocomposite for the loading−unloading cycles at a series of set strains (10−50%). The stress−strain ($\sigma-\varepsilon$) curves obtained during the loading process could be divided into three characteristic distinct stages: a linear elastic region for $\varepsilon < 12\%$ with an elastic modulus of ~3 kPa, a plateau region for $12\% < \varepsilon < 40\%$, and a densification region for $\varepsilon > 40\%$ with a steeply increased slope.[28] The σ of unloading curves could almost return to the original points after unloading for each ε, indicating that the rGO/PI composites completely recover their original sizes without plastic deformations. Such distinct deformation behaviors are typically observed in open-cell foams.[29] The energy loss coefficient (η), which is defined as the loop area relative to the area under the loading curve,[30] gradually increases with the increase of strain (Figure 3, panel a, inset). The hysteresis curves of rGO/PI monolith for 2000 loading−unloading cycles with a maximum strain of 50% are obtained in Figure 3, panel b. The nanocomposite exhibits no significant plastic deformation, which implies their structural robustness. During 2000 fatigue cycles, the coefficient decreases and gradually stabilizes (Figure 3b, inset). Furthermore, the obtained stress−strain curves almost overlap each other when the rGO/PI monolith is compressed at different strain rates (10%−1000%/min), which highlights that the hysteresis can be maintained upon fast deformation (Figure 3c). As for the coefficient at each strain rate (Figure 3c, inset), it reaches a maximum value (η = 42.7%) at strain rates of 10%/min and decreases with the increase of strain rate (η = 36.9%, 1000%/min). Moreover, as presented in Figure3, panel d, there is slight decrease in the stiffness or strength for the rGO/PI composite after 2000 loading−unloading fatigue cycles. However, the maximum stress can still retain over 88%, and the total strain has a slight decrease of 3%, which tends to be stable within 2000 cycles. Additionally, the rGO/PI nanocomposite was subjected to a tensile test (Figure3e). The tensile $\sigma-\varepsilon$ curve displays that the composite has a

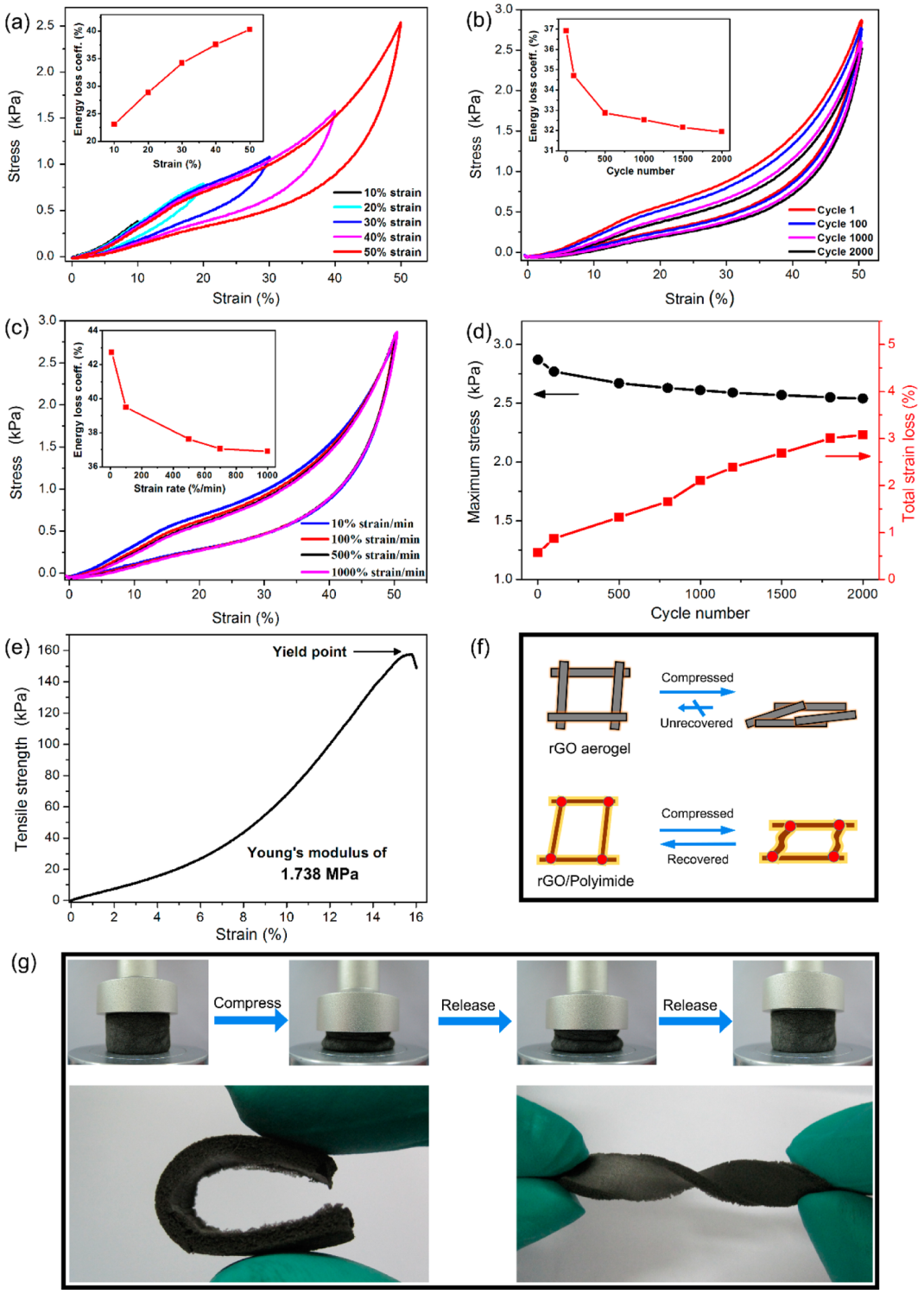

Figure 3. (a) The stress−strain ($\sigma-\varepsilon$) curves of rGO/PI nanocomposite with different set strains. Inset: calculated energy loss coefficients of rGO/PI nanocomposite compressed to different strains. (b) Fatigue test of rGO/PI nanocomposite at 50% strain for 2000 cycles. Inset: energy loss coefficients over 2000 cycles. (c) $\sigma-\varepsilon$ curves tested under different strain rates. Inset: energy loss coefficients of different strain rates. (d) Retention of maximum stress at 50% strain and total loss during 2000 cycles (calculated from the $\sigma-\varepsilon$ curves expressed in panel b). (e) Tensile $\sigma-\varepsilon$ curve for the rGO/PI. (f) The compressive schematic of rGO aerogel and rGO/PI nanocomposite. (g) A set of digital images shows the recovering process of a compressed rGO/PI nanocomposite and the high levels deformation of bend and torsion.

robust Young's modulus of 1.738 MPa, and its maximum yield value is measured to be 157.3 kPa, indicating the high toughness of the nanocomposite.

To further assess the structure and properties of the rGO/PI nanocomposite, controlled experiments of compression were performed among neat rGO

aerogel, pure PI monolith, and rGO/PI nanocomposite, respectively. The digital photographs of deformation tests vividly demonstrate the enhancement of mechanical properties by the cooperative effect between rGO and PI (Figure 3g, Figure S4). Neat rGO aerogel obtained by the same protocol could demonstrate 3D architectures (Figure 2a). However, the aerogel exhibits weak elasticity and toughness. After the compression test, the normal rGO aerogel is not able to recover its initial shape and deforms permanently due to the flexibility of graphene sheets (Figure 3f, Figure S4a).[9] Strikingly, contrary to a fragile and permanently collapsed rGO aerogel, the novel rGO/PI nanocomposite could withstand a high level of compression due to the strong interactions between rGO and PI (Figure 3f, Figure 3g, top) even compressed at a large ε of 90%. Once the compression stress was removed, it completely and rapidly recovered its original shape with no damage or rupture. In comparison, pure PI monolith displayed a plastic deformation of ~4% at ε = 50%, which was a typical characteristic of polymeric foams (Figure S4b).[28]

In addition to the super recyclable compressibility, the as-prepared rGO/PI nanocomposite can also stand up to a high level of deformations such as bending and torsion (Figure 3g). The rGO/PI nanocomposite could be bent even to nearly 180 degrees. Moreover, the ribbon-like sample of rGO/PI can be twisted largely. These performances reveal the excellent mechanical flexibility of our nanocomposite. Compared with other graphene-based strain sensors, the rGO/PI nanocomposite exhibited excellent flexibility (Table S1). Notably, the rGO/PI nanocomposite revealed excellent flexible and elastic properties, thus holding great potential as strain sensors, especially upon the deformations of bending, stretching, and torsion. Unfortunately, up to now there has been no report to present the flexible strain sensors, especially upon bending, stretching, and torsion.

We contributed the mechanical properties of rGO/PI monoliths to the synergistic effect between rGO sheets and PI building blocks. The strong interactions between GO flakes and PAA building blocks result in a fairly uniform distribution of rGO sheets in GO/PAA porous framework. Both PAA building blocks and GO sheets form a highly porous interconnected morphology and prevent them from crumbling during the freeze-drying procedure. After the amidation process, the cooperative effect between rGO sheets and PI building blocks reinforces the toughness of rGO/PI co-organized nanocomposite and endows it with excellent elasticity. Upon loading, the load is effectively transferred between rGO sheets and PI building blocks under deformations. After removal of the loading, the rGO/PI skeletons recover to their initial interconnected morphology, allowing the nanocomposites to return their original sizes.

The advantage of the unique binary-network structure combined with the merits of PI and graphene endows the rGO/PI composites suitable for applications as flexible and compressible conductor. The rGO/PI monoliths with 5 wt % GO sheets were chosen to make compressible conductors. The composites present an electrical conductivity of $\sim 2.2 \times 10^{-2}$ S m^{-1}, which is four orders of magnitude higher than the graphene-based composite ($\sim 10^{-6}$ S m^{-1}).[31]

To demonstrate the excellent pressure-responsive properties of rGO/PI monoliths, the electronic resistance variation ratios ($\Delta R/R_0 = (R_0 - R_P)/R_0$; R_0 and R_P correspond to the resistance without and with stress, respectively) with respect to the strain were investigated. The top and bottom surfaces of rGO/PI cylinder samples were treated by the conductive silver paint, respectively, where two silver wires were connected to an electrochemical workstation. As presented in Figure 4, panel a, the pressure sensitivity (S) of the rGO/PI nanocomposite is calculated on the basis of measured values, which can be defined as $S = \delta(\Delta R/R_0)/\delta P$.[16] The plot of curves show two characteristic stages corresponding to differences in sensitivity. The low-pressure regime from 0−1.5 kPa exhibits an increased slope with a sensitivity of 0.18 kPa^{-1}, while in the large-pressure regime (3.5−6.5 kPa), the sensitivity of rGO/PI composite is 0.023 kPa^{-1}. Owing to the tunneling of charged carries between adjacent rGO sheets in the nanocomposite, the resistance exponentially decreases when the average distance between graphene sheets reduces during the loading procedure, which gives rise to a corresponding current enhancement (Figure 4a, inset).[32] When suffered from a wide range of compressive strains during the loading and unloading process, the variation of electronic resistance of rGO/PI nanocomposite synchronizes with the change of applied strains (Figure 4b). When compression strain is 10%, the variation ratio of electronic resistance has a change of 9.96% (almost approaching 10%). This relationship is confirmed to be linear. With the increase of applied strains from 20% to 50%, the change in resistance variation ratios for rGO/PI composite is about 17.9%, 27.0%, 37.6%, and 49.3%, respectively. To demonstrate the retention property in resistance of the rGO/PI nanocomposite, we tested the retention of change in resistance by retaining a 1.5 kPa stress and 0 kPa stress for ten seconds each time during the cycles of loading−unloading process.[17] As revealed in Figure 4, panel c, the plot of change in resistance as a function of time, which is in accordance with the stress−time curve, maintains a distinct plateau regime until the applied stress is released. The cycling stability of as-formed rGO/PI monolith was investigated (Figure 4d). Even after 2000 loading−unloading cycles, the variation of electronic resistance displays reasonably excellent repeatability, and the resistance of rGO/PI sample exhibits no significant decrease. Thus, it is shown that our fabricated rGO/PI composite has long lifetime and cycling stability.

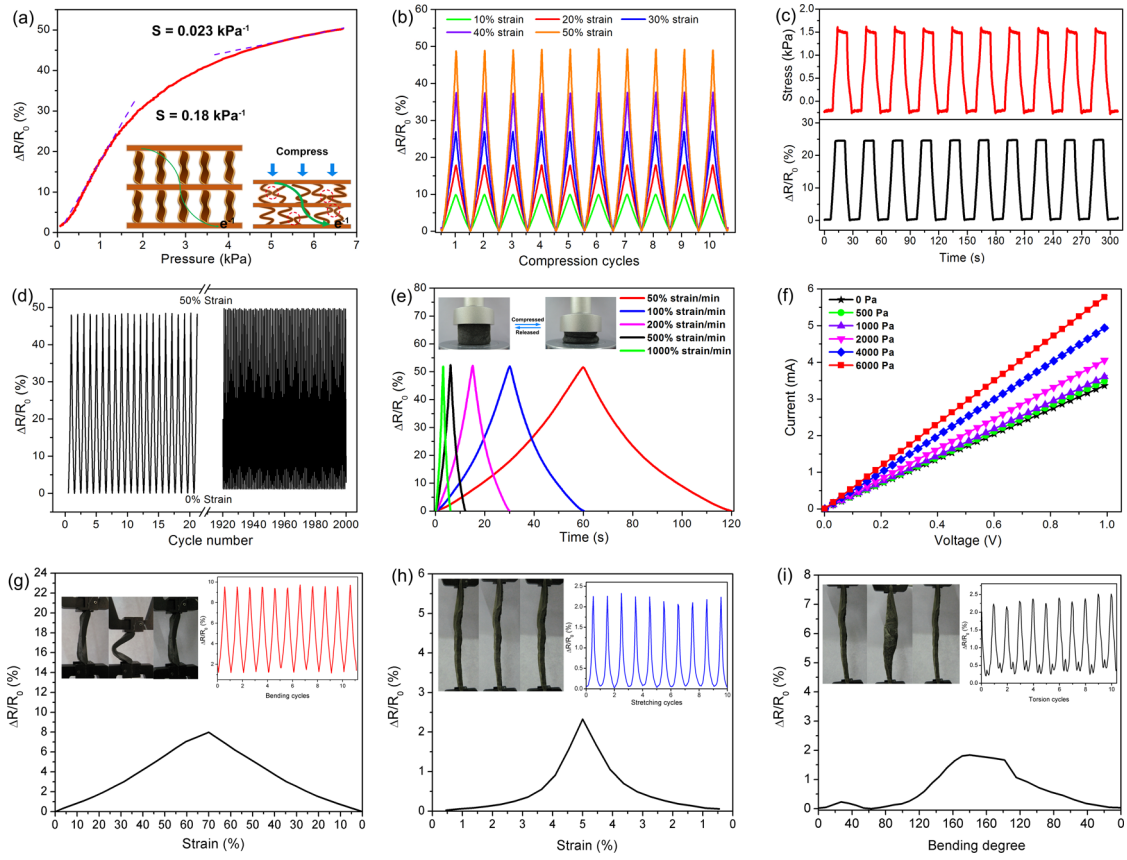

Figure 4. (a) Pressure−response curves for rGO/PI nanocomposite. Inset: current changes in responses to compress and release. (b) Multiple-cycle tests of change in resistance with different applied strains. (c) The time retention curve of change in resistance with time and stress with time. (d) Cycling stability test of rGO/PI composite under repeated applied strain of 50% for 2000 cycles. (e) Variation of the resistance of the rGO/PI composite with the strain of 50% under different strain rates (50−1000%/min). (f) Current−voltage of rGO/PI nanocomposite under different applied stress. (g) The resistance variation of the rGO/PI nanocomposite in a typical bending cycle. The strain refers to $\Delta L/L_0 = (L_0 - L_P)/L_0$, where L_0 and L_P denote the distance between two ends of the nanocomposite without and with applied pressure, respectively. Inset: electrical-resistance change of rGO/PI nanocomposite under mechanical deformation of bending and then straightening for each cycle. Photographs of the bending process. (h) Electrical-resistance change of rGO/PI nanocomposite as a function of stretching strain of 5%. Inset: electrical-resistance variation of rGO/PI nanocomposite after 5% stretching and then releasing for each cycle. Photographs of the stretching process. (i) Electrical-resistance variation of rGO/PI nanocomposite in a typical torsion cycle. Inset: electrical-resistance variation of rGO/PI nanocomposite after 180 degree torsion and then releasing for each cycle. Photographs of the torsion process.

Furthermore, there is an almost perfectly linear relationship between the variation of resistance and the applied strain at different compression rates (Figure 4e). Moreover, we measured the current−voltage curves of rGO/PI nanocomposite for different levels of applied stress (Figure 4f), which implied the fine linear current−voltage characteristics of the sample. In addition, the bending, stretching, and torsion tests were also carried out to further study the mechanical and electrical properties of rGO/PI nanocomposite. As shown in Figure 4, panel g, note that the resistance variation expresses an increase of ∼9% at the strain of 70% and can completely return to original structure after straightening (the strain refers to $\Delta L/L_0 = (L_0 - L_P)/L_0$, where L_0 and L_P denote the distance between two ends of the nanocomposite without and with applied pressure, respectively). The bending cycles become stable, and the resistance variation remains constant, indicating extraordinary electromechanical stability of the rGO/PI nanocomposite (Figure 4g, inset). The electrical resistance change under stretching deformation was also measured. As depicted in Figure 4, panel h, the resistance variation is investigated as a function of uniaxial tensile stain, which shows a slight increase of ∼2.2% under 5% stretching. Similar to the research results of bending cycles, the resistance variation remains stable during the stretching cycles (Figure 4h, inset). Notably, the rGO/PI nanocomposite can even give a significant output signal of electrical-resistance variation under deformation of torsion (Figure 4i). The electrical-resistance change of the rGO/PI nanocomposite exhibits nonlinear increase with increasing torsion degree. Moreover, the changes in resistance express fine repeatability during the cyclic deformations of torsion (Figure 4i, inset). These results reveal the excellent electromechanical properties of rGO/PI. To our knowledge, very few graphene-based aerogels can keep from crumping

and return to their original structure after suffering such cyclic deformations of bending, stretching, and torsion. There have been almost no reports about the electrical-resistance change of graphene-based aerogels under these mechanical deformations. These merits are deemed to be attributed to the 3D binary-network, desirable electrical conductivity, and excellent mechanical properties of the nanocomposites. All results suggest that our prepared rGO/PI foams have high electromechanical stability and hold great potential for the applications as multifunctional strain sensors under the deformations of compression, bending, stretching, and torsion.

CONCLUSIONS

In summary, we have demonstrated that the mechanically fragile rGO aerogel can be transformed into super flexible and elastic nanocomposite foam by introducing water-soluble PI precursor. The synergistic effect between rGO and PI endows the elastomer with desirable electrical conductivity, remarkable compression sensitivity, and excellent durable stability. Our rGO/PI nanocomposites may provide new insights into the 3D macroscopic graphene design and open a new route to explore widespread applications in multifunctional strain sensors under the deformations of compression, bending, stretching, and torsion.

MATERIALS AND METHODS

Material. The 4,4′-diaminodiphenyl ether (ODA, 98%), pyromellitic dianhydride (PMDA,99%), N,N-dimethylacetamide (DMAc, 99%), triethylamine (TEA, 99%), $KMnO_4$, H_2SO_4 (98%), H_3PO_4 (85%), H_2O_2 (30%), and HCl (37%) were purchased from Sinopharm Chemical Reagent Co., Ltd. Natural graphite powder (325 mesh) was provided by Alfa-Aesar. All these reagents were used without further purification.

Synthesis of Water-Soluble Polyimide Precursor Solution. Water-soluble PI precursor solution was synthesized according to the literature (Scheme S1).[19] The 4,4′- ODA was dispersed in DMAc with a magnetic stirrer. Then, a quantity of PMDA was dissolved into the mixture with vigorous stirring for 5 h to obtain PAA solution. Note that the PMDA/4,4′- ODA molar ratio was 100:99. The resultant solution was poured into excessive deionized water, and the produced precipitate was filtrated, washed, and dried to move the residual deionized water. After that, the ammonium salt solution of PAA with a solid content of 5 wt % was prepared from PAA (1 g) and TEA (0.48g) in deionized water (18.52 mL) with stirring for 5 h at room temperature. Finally, the water-soluble polyimide precursor solution was obtained for further use.

Preparation of Graphene Oxide. GO was synthesized by oxidizing expandable graphite (EG) powder based on the modified Hummers method.[20] EG powder (3 g) was mixed with a mixture of concentrated H_2SO_4/H_3PO_4 (360:40 mL) and $KMnO_4$ (18 g). After reaction at 50 °C for 10 h, the mixture was cooled to room temperature, poured into an ice bath (500 mL), and further treated with H_2O_2 (30%, 5 mL). Bright-yellow suspension was treated by filtration, and the resulting solid material was washed in succession with 10% HCl and deionized water by centrifugation (9500 rpm for 1 h) to remove SO_4^{2-} and Cl^-. GO sheets were collected and then diluted to a desired concentration.

Preparation of rGO/PI Nanocomposite. The rGO/PI nanocomposite sponge was fabricated by means of two steps of freeze-drying and thermal annealing method. Typically, the water-soluble polyimide precursor solution was mixed with a quantity of GO aqueous dispersion (5 mg/mL), and the volume ratio of ammonium salt solution of PAA to GO aqueous dispersion was 4:1. The mixture was continually stirred for 2 h followed by lyophilizing in a freeze-dryer for 24 h. The obtained monolith was then sequentially subjected to thermal annealing at 300 °C in argon atmosphere for 2 h. Monolithic rGO/PI nanocomposites with different shapes were synthesized under the same conditions by adjusting the mold. Pure polyimide sponges and graphene aerogels were obtained by the same procedure.

Pressure Sensitivity Characterization. To evaluate the properties of pressure sensitivity, the electronic resistance variation ratios ($\Delta R/R_0$) were chosen to express the change of current during different pressures in the deformation process. Therefore, the pressure sensitivity of rGO/PI nanocomposite can be calculated as follows:

$$\Delta R/R_0 = (R_0 - R_P)/R_0 \quad (1)$$

$$S = \delta(\Delta R/R_0)/\delta P \quad (2)$$

Where R_0 and R_P are the resistance without and with applied pressure, respectively. The $\Delta R/R_0$ was plotted as a function of compressive pressure. S is defined as the pressure sensitivity, which can be obtained from the slope of curves ($\Delta R/R_0$ pressure), and P denotes the applied pressure. The reversible compressibility of the rGO/PI nanocomposite could also be evaluated by the stability of electronic resistance variation ratios when the nanocomposite was under cyclic compression.

Conflict of Interest: The authors declare no competing financial interest.

Acknowledgment. Yibin, Li and Xiaodong, He acknowledge the Natural Science Foundation in China (NSFC 11272109) and the Ph. D. Programs Foundation of Ministry of Education of China (20122302110065). We are grateful for the constructive comments and valuable advice from all the reviewers for further improvement of our work.

Supporting Information Available: The Supporting Information is available free of charge on the ACS Publications website at DOI: 10.1021/acsnano.5b02781.

Schematic of synthesis process, table of comparison of graphene-based strain sensors, additional photographs, figures (PDF)

REFERENCES AND NOTES

1. Boehm, H.-P. Graphene—How a Laboratory Curiosity Suddenly Became Extremely Interesting. *Angew. Chem., Int. Ed.* **2010**, *49*, 9332–9335.
2. Geim, A. K. Graphene: Status and Prospects. *Science* **2009**, *324*, 1530–1534.
3. Park, S.; Ruoff, R. S. Chemical Methods for the Production of Graphenes. *Nat. Nanotechnol.* **2009**, *4*, 217–224.
4. Xu, Y.; Sheng, K.; Li, C.; Shi, G. Self-Assembled Graphene Hydrogel *via* a One-Step Hydrothermal Process. *ACS Nano* **2010**, *4*, 4324–4330.
5. Bi, H.; Xie, X.; Yin, K.; Zhou, Y.; Wan, S.; He, L.; Xu, F.; Banhart, F.; Sun, L.; Ruoff, R. S. Spongy Graphene as a Highly Efficient and Recyclable Sorbent for Oils and Organic Solvents. *Adv. Funct. Mater.* **2012**, *22*, 4421–4425.
6. Zhao, Y.; Hu, C.; Hu, Y.; Cheng, H.; Shi, G.; Qu, L. A Versatile, Ultralight, Nitrogen-Doped Graphene Framework. *Angew. Chem., Int. Ed.* **2012**, *51*, 11371–11375.
7. Hu, H.; Zhao, Z. B.; Wan, W. B.; Gogotsi, Y.; Qiu, J. S. Ultralight and Highly Compressible Graphene Aerogels. *Adv. Mater.* **2013**, *25*, 2219–2223.

8. Qiu, L.; Liu, J. Z.; Chang, S. L. Y.; Wu, Y.; Li, D. Biomimetic superelastic graphene-based cellular monoliths. *Nat. Commun.* **2012**, *3*, 1241.
9. Sun, H.; Xu, Z.; Gao, C. Multifunctional, Ultra-Flyweight, Synergistically Assembled Carbon Aerogels. *Adv. Mater.* **2013**, *25*, 2554–2560.
10. Barg, S.; Perez, F. M.; Ni, N.; do Vale Pereira, P.; Maher, R. C.; Garcia-Tuñon, E.; Eslava, S.; Agnoli, S.; Mattevi, C.; Saiz, E. Mesoscale Assembly of Chemically Modified Graphene into Complex Cellular Networks. *Nat. Commun.* **2014**, *5*, 4328.
11. Kuang, J.; Liu, L.; Gao, Y.; Zhou, D.; Chen, Z.; Han, B.; Zhang, Z. A Hierarchically Structured Graphene Foam and its Potential as a Large-Scale Strain-Gauge Sensor. *Nanoscale* **2013**, *5*, 12171–12177.
12. Chen, Z.; Ren, W.; Gao, L.; Liu, B.; Pei, S.; Cheng, H.-M. Three-Dimensional Flexible and Conductive Interconnected Graphene Networks Grown by Chemical Vapour Deposition. *Nat. Mater.* **2011**, *10*, 424–428.
13. Yavari, F.; Chen, Z.; Thomas, A. V.; Ren, W.; Cheng, H.-M.; Koratkar, N. High Sensitivity Gas Detection Using a Macroscopic Three-Dimensional Graphene Foam Network. *Sci. Rep.* **2011**, *1*, 166.
14. Peng, Q.; Li, Y.; He, X.; Gui, X.; Shang, Y.; Wang, C.; Wang, C.; Zhao, W.; Du, S.; Shi, E.; *et al*. Graphene Nanoribbon Aerogels Unzipped from Carbon Nanotube Sponges. *Adv. Mater.* **2014**, *26*, 3241–3247.
15. Wu, C.; Huang, X.; Wu, X.; Qian, R.; Jiang, P. Mechanically Flexible and Multifunctional Polymer-Based Graphene Foams for Elastic Conductors and Oil-Water Separators. *Adv. Mater.* **2013**, *25*, 5658–5662.
16. Yao, H.-B.; Ge, J.; Wang, C.-F.; Wang, X.; Hu, W.; Zheng, Z.-J.; Ni, Y.; Yu, S.-H. A Flexible and Highly Pressure-Sensitive Graphene–Polyurethane Sponge Based on Fractured Microstructure Design. *Adv. Mater.* **2013**, *25*, 6692–6698.
17. Samad, Y. A.; Li, Y.; Schiffer, A.; Alhassan, S. M.; Liao, K. Graphene Foam Developed with a Novel Two-Step Technique for Low and High Strains and Pressure-Sensing Applications. *Small* **2015**, *11*, 2380–2385.
18. Yoonessi, M.; Shi, Y.; Scheiman, D. A.; Lebron-Colon, M.; Tigelaar, D. M.; Weiss, R. A.; Meador, M. A. Graphene Polyimide Nanocomposites; Thermal, Mechanical, and High-Temperature Shape Memory Effects. *ACS Nano* **2012**, *6*, 7644–7655.
19. Zhang, Y.; Fan, W.; Huang, Y.; Zhang, C.; Liu, T. Graphene/Carbon Aerogels Derived from Graphene Crosslinked Polyimide as Electrode Materials for Supercapacitors. *RSC Adv.* **2015**, *5*, 1301–1308.
20. Marcano, D. C.; Kosynkin, D. V.; Berlin, J. M.; Sinitskii, A.; Sun, Z.; Slesarev, A.; Alemany, L. B.; Lu, W.; Tour, J. M. Improved Synthesis of Graphene Oxide. *ACS Nano* **2010**, *4*, 4806–4814.
21. Wang, C.; He, X.; Shang, Y.; Peng, Q.; Qin, Y.; Shi, E.; Yang, Y.; Wu, S.; Xu, W.; Du, S.; *et al*. Multifunctional Graphene Sheet-Nanoribbon Hybrid Aerogels. *J. Mater. Chem. A* **2014**, *2*, 14994–15000.
22. Deville, S.; Saiz, E.; Nalla, R. K.; Tomsia, A. P. Freezing as a Path to Build Complex Composites. *Science* **2006**, *311*, 515–518.
23. Ramanathan, T.; Abdala, A. A.; Stankovich, S.; Dikin, D. A.; Herrera Alonso, M.; Piner, R. D.; Adamson, D. H.; Schniepp, H. C.; ChenX; Ruoff, R. S.; *et al*. Functionalized Graphene Sheets for Polymer Nanocomposites. *Nat. Nanotechnol.* **2008**, *3*, 327–331.
24. Ramakrishnan, S.; Dhakshnamoorthy, M.; Jelmy, E. J.; Vasanthakumari, R.; Kothurkar, N. K. Synthesis and Characterization of Graphene Oxide-Polyimide Nanofiber Composites. *RSC Adv.* **2014**, *4*, 9743–9749.
25. Xu, X.; Li, H.; Zhang, Q.; Hu, H.; Zhao, Z.; Li, J.; Li, J.; Qiao, Y.; Gogotsi, Y. Self-Sensing, Ultralight, and Conductive 3D Graphene/Iron Oxide Aerogel Elastomer Deformable in a Magnetic Field. *ACS Nano* **2015**, *9*, 3969–3977.
26. Hong, J.-Y.; Bak, B. M.; Wie, J. J.; Kong, J.; Park, H. S. Reversibly Compressible, Highly Elastic, and Durable Graphene Aerogels for Energy Storage Devices under Limiting Conditions. *Adv. Funct. Mater.* **2015**, *25*, 1053–1062.
27. Ektessabi, A. M.; Hakamata, S. XPS Study of Ion Beam Modified Polyimide Films. *Thin Solid Films* **2000**, *377–378*, 621–625.
28. Kim, K. H.; Oh, Y.; Islam, M. F. Graphene Coating Makes Carbon Nanotube Aerogels Superelastic and Resistant to Fatigue. *Nat. Nanotechnol.* **2012**, *7*, 562–566.
29. Gibson, L. J.; Ashby, M. F. *Cellular Solids: Structure and Properties*; Cambridge University Press: Cambridge, U.K., 1997.
30. Zhao, W.; Li, Y.; Wang, S.; He, X.; Shang, Y.; Peng, Q.; Wang, C.; Du, S.; Gui, X.; Yang, Y.; *et al*. Elastic Improvement of Carbon Nanotube Sponges by Depositing Amorphous Carbon Coating. *Carbon* **2014**, *76*, 19–26.
31. Yoonessi, M.; Gaier, J. R. Highly Conductive Multifunctional Graphene Polycarbonate Nanocomposites. *ACS Nano* **2010**, *4*, 7211–7220.
32. Zhao, J.; Wang, G.; Yang, R.; Lu, X.; Cheng, M.; He, C.; Xie, G.; Meng, J.; Shi, D.; Zhang, G. Tunable Piezoresistivity of Nanographene Films for Strain Sensing. *ACS Nano* **2015**, *9*, 1622–1629.
33. Park, O.-K.; Hahm, M. G.; Lee, S.; Joh, H.-I.; Na, S.-I.; Vajtai, R.; Lee, J. H.; Ku, B.-C.; Ajayan, P. M. In Situ Synthesis of Thermochemically Reduced Graphene Oxide Conducting Nanocomposites. *Nano Lett.* **2012**, *12*, 1789–1793.